Global and Planetary Change 217 (2022) 103918

Contents lists available at ScienceDirect

Global and Planetary Change

journal homepage: www.elsevier.com/locate/gloplacha

Response of calcareous nannoplankton to the Paleocene–Eocene Thermal Maximum in the Paratethys Seaway (Tarim Basin, West China)

Yasu Wang [a,b], Ying Cui [c], Hong Su [d], Jingxin Jiang [e], Yang Wang [f], Zhilin Yang [g], Xiumian Hu [e], Shijun Jiang [a,b,*]

[a] College of Oceanography, Hohai University, Nanjing 210024, China
[b] Southern Marine Science and Engineering Guangdong Laboratory (Zhuhai), Zhuhai 519080, China
[c] Department of Earth and Environmental Studies, Montclair State University, Montclair, NJ 07043, USA
[d] College of Life Science and Technology, Jinan University, Guangzhou 510632, China
[e] State Key Laboratory of Mineral Deposit Research, School of Earth Sciences and Engineering, Nanjing University, Nanjing 210023, China
[f] Department of Earth, Ocean & Atmospheric Science and National High Magnetic Field Laboratory, Florida State University, Tallahassee, FL 32306, USA
[g] Exploration and Development Research Institute, Tarim Oilfield Company, PetroChina, Korla 841000, Xinjiang, China

ARTICLE INFO

Editor: Dr. Maoyan Zhu

Keywords:
Calcareous nannofossil
Paleocene–Eocene thermal Maximum
Epicontinental seaway
Paratethys
Tarim Basin

ABSTRACT

The Paleocene-Eocene Thermal Maximum (PETM) was a rapid global warming occurred 56 million years ago and has been widely viewed as an ancient analogue to the ongoing warming driven by anthropogenic CO_2 emissions. The complete and continuous Paleogene shallow marine strata well preserved and outcropped in the Tarim Basin, northwestern China are ideal to study the paleoenvironmental change of the Paratethys Seaway during the PETM. To date, no high-resolution calcareous nannofossil biostratigraphy has been performed for the PETM interval in the Tarim Basin. Outcrop samples taken from the Qimugen Formation in the Kuzigongsu section contain abundant, moderately well preserved calcareous nannofossils, allowing for the establishment of a high-resolution biostratigraphic framework. Overall, 73 species of calcareous nannofossils from 33 genera were observed, with the dominant species including *Coccolithus pelagicus*, various *Toweius* species, *Pontosphaera exilis*, and *Micrantholithus flos.* The five calcareous nannofossil datums allow for the recognization of nannofossil Zone NP6 through Zone NP10. The common occurrence of shallow-water taxa (*Micrantholithus*) throughout the section suggests a middle to outer neritic setting as the depositional environment of the Kuzigongsu section. The stratigraphic distribution of "excursion taxa" (*Coccolithus bownii, Discoaster araneus*, *D. acutus, Rhomboaster* spp.) is consistent with the range of negative excursions in $\delta^{13}C_{carb}$ and $\delta^{18}O_{carb}$, indicating that these "excursion taxa" are micropaleontological markers for identifying the presence of the PETM in the Paratethys Seaway. During the PETM, the deteriorated preservation and extremely low abundance of nannofossils and near-zero wt% $CaCO_3$ values suggest that ocean acidification occurred in the shallow water of the Paratethys Seaway. In addition, a significant increase in the species *Neochiastozygus junctus*, which is a high productivity indicator suggests increased surface ocean productivity. Higher primary productivity may be triggered by enhanced continental weathering delivering increased nutrient through river runoff.

1. Introduction

The Paleocene–Eocene Thermal Maximum (PETM), occurred at approximately 56 Ma and lasted for ~150–220 kyr (Röhl et al., 2007; Westerhold et al., 2012), has received considerable attention in the last 30 years (Kennett and Stott, 1991; Bralower et al., 1995; Thomas and Shackleton, 1996; Zachos et al., 2003; Self-Trail et al., 2017). The PETM is associated with prominent global negative carbon isotope excursion (CIE, 3–6‰) and 5–9 °C warming globally (see McInerney and Wing, 2011 for a review), and shares many similarities to the ongoing climate change due to anthropogenic fossil fuel combustion (IPCC, 2013; Zeebe et al. (2016). The rate of carbon emissions during the PETM was about ten times slower than the current anthropogenic carbon release (Cui et al., 2011; Zeebe et al., 2016). The estimated cumulative amount of carbon released during the PETM ranges from ~2000 to >13,000 Pg C (Panchuk et al., 2008; Cui et al., 2011; Gutjahr et al., 2017).

* Corresponding author at: College of Oceanography, Hohai University, Nanjing 210024, China.
E-mail addresses: ssj0047@my.fsu.edu, sjiang@hhu.edu.cn (S. Jiang).

https://doi.org/10.1016/j.gloplacha.2022.103918
Received 31 January 2022; Received in revised form 9 August 2022; Accepted 10 August 2022
Available online 25 August 2022

Despite the differences in the environmental conditions between the late Paleocene and today (i.e., late Paleocene was ice free in polar regions), the PETM is arguably considered as one of the best analogs to understand the impact of rapid and massive carbon addition, global warming, and ocean acidification (Zachos et al., 2005; Zeebe et al., 2014; Kiehl et al., 2018). The climatic, marine biological and geochemical impacts of the PETM were manifested as a large-scale extinction of benthic foraminifera (Thomas and Shackleton, 1996; Thomas, 2007; Alegret et al., 2009; Keller et al., 2018), ocean acidification (Zachos et al., 2005; Penman et al., 2014; Bralower et al., 2018), intensified hydrological cycle (Bowen et al., 2004; Handley et al., 2012; Carmichael et al., 2017), turnover of calcareous nannoplankton (Gibbs et al., 2006a; Lei et al., 2016), an increase in dinoflagellate *Apectodinium* (Crouch et al., 2003) and ocean deoxygenation (Zhou et al., 2014; Yao et al., 2018). On land, biotic response to the PETM was associated with mammal migrations (Smith et al., 2006) and mammalian dwarfing due to extreme warmth (Secord et al., 2012). These various environmental processes involved are particularly difficult to disentangle and their expressions in the sedimentary records likely vary in different regions (Dickson et al., 2014).

Since its discovery in the deep-sea sediments by Kennett and Stott (1991), >150 locations worldwide have been documented that record the PETM, with depositional environments ranging from continental interior to abyssal ocean (McInerney and Wing, 2011; Carmichael et al., 2017). Most records are from a deep-sea setting or from the terrestrial realm with only a limited number of shallow marine PETM sections reported (Speijer and Schmitz, 1998; Speijer and Wagner, 2002). The existing shallow marine records are mainly distributed in the western Tethys and the mid-Atlantic Coastal Plain (e.g. Stassen et al., 2012; Self-Trail et al., 2012; Lyons et al., 2019), and there is still a scarcity of detailed research in the Paratethys Seaway.

The semi-closed Paratethys Seaway is considered as a critical site for the formation of warm and saline intermediate water due to intense evaporation (Sagoo et al., 2013; Zhu et al., 2020). It is also thought to be an important moisture source for the Eurasian landmass (Ramstein et al., 1997; Zhang et al., 2007; Zhu et al., 2019). Burial of organic matter may have been enhanced along the shallow continental margins of the Paratethys Seaway due to increased upwelling of low-oxygen intermediate water (Speijer and Wagner, 2002; Dickson et al., 2014). This makes the Paratethys a key region for understanding the mechanisms that drove the PETM (Kennett and Stott, 1991). However, unequivocal PETM records from the Paratethys are sparse, and the existing shallow marine records have low temporal resolution and/or poor age constraint, or are truncated, leaving a major gap in understanding of this climatically sensitive and ecologically fragile region (Li et al., 2017; Zhang et al., 2017; Cao et al., 2018; Li et al., 2021). Moreover, few sea surface temperature data are available and general circulation models simulate varying magnitude of temperature anomalies in the Paratethys during the PETM (Winguth et al., 2010; Zhu et al., 2019). These limitations hamper a thorough understanding of the effects of warming and ocean acidification on the shallow marine ecosystem.

In this study, we examine in detail a newly discovered shallow marine PETM section from the Paratethys Seaway located in the western Tarim Basin, northwestern China (Fig. 1). We attempt to: (1) document the high-resolution PETM biostratigraphic record using calcareous nannofossils and bulk carbon and oxygen isotopes from marine carbonates; (2) explore the environmental impact from greenhouse gas forcing in the Paratethys during the PETM; and (3) compare the characteristics of the Paratethys to other shallow marine PETM sites in the western Tethys and mid-Atlantic Coastal Plains.

2. Geological background

2.1. Regional geology

The Tarim Basin is a northwestward trending rhombic-shaped depression covering an area of 563,000 km^2. It lies in the Xinjiang Uygur Autonomous Region in NW China (37°10′– 42°00′ N, 75°00′–93°00′ E) and is surrounded by the West Kunlun mountains to the west, the Altyn Tagn mountains to the south and the Tien Shan to the north (Fig. 1). The center of the basin is mostly covered by the Taklimakan Desert. The average elevation of the basin floor is 1200 m above sea level (asl) and Cretaceous–Paleogene marine rocks crop out on the fringes of the basin usually at >2000 m asl. The Paleozoic sediments of the Tarim Basin are widespread and primarily consist of platform carbonates and fine-grained clastic rocks (Carroll et al., 1995), whereas coarse-grained fluvial and lacustrine sequences are dominant during the Mesozoic and Cenozoic (He et al., 2005; Bosboom et al., 2014).

Marine deposition initiated in the Tarim Basin in the Late Cretaceous and occurred intermittently throughout the Paleogene (Zhong, 1984; Tang, 1992; Burtman, 2000; Zhang et al., 2018; Wang et al., 2022), during which a shallow epicontinental sea known as the Paratethys connected central Eurasia to the western Mediterranean Tethys (Mao and Norris, 1984; Tang, 1992; Bosboom et al., 2011). This epicontinental sea retreated westward after five successive marine transgressions through the present-day Alai Valley (Bosboom et al., 2014), eventually separating the western Tethys and the Arctic Sea during the latest Eocene to early Oligocene, and becoming the remnant Paratethys Seaway (Figs. 1 and 2). The largest transgression occurred across the Paleocene-Eocene boundary, when the Paratethys was a restricted

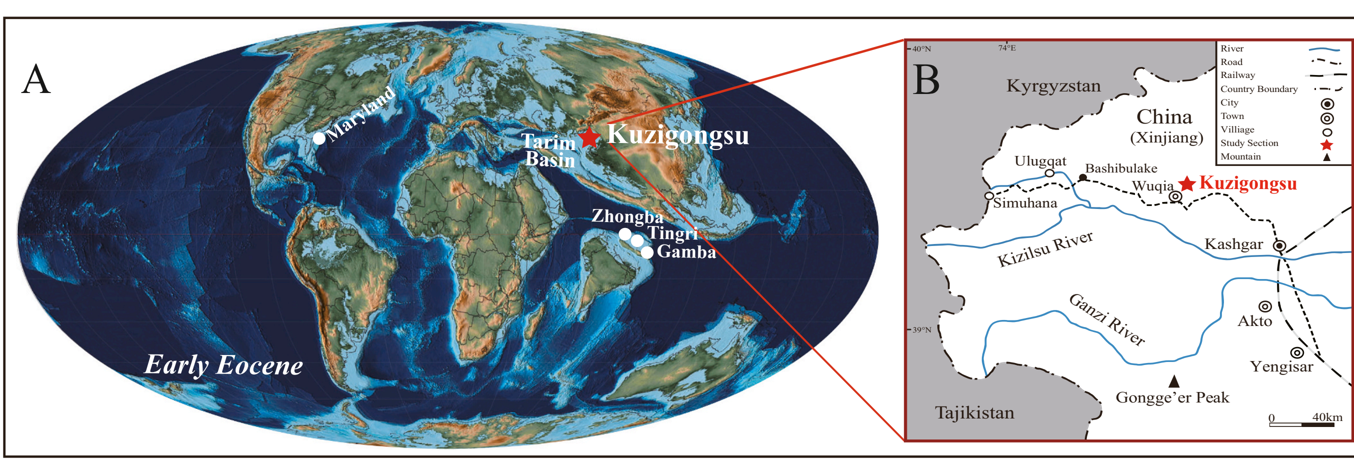

Fig. 1. A) Paleogeographic setting of the study area in the early Eocene (after Scotese, 2014); B) present location of the Kuzigongsu section (after Cao et al., 2018). Also shown are other shallow water PETM records in southern Tibet (Li et al., 2017, 2020, 2022; Zhang et al., 2019; Jiang et al., 2021), Tarim Basin (Cao et al., 2018; Li et al., 2020), and Maryland, USA (Self-Trail et al., 2012).

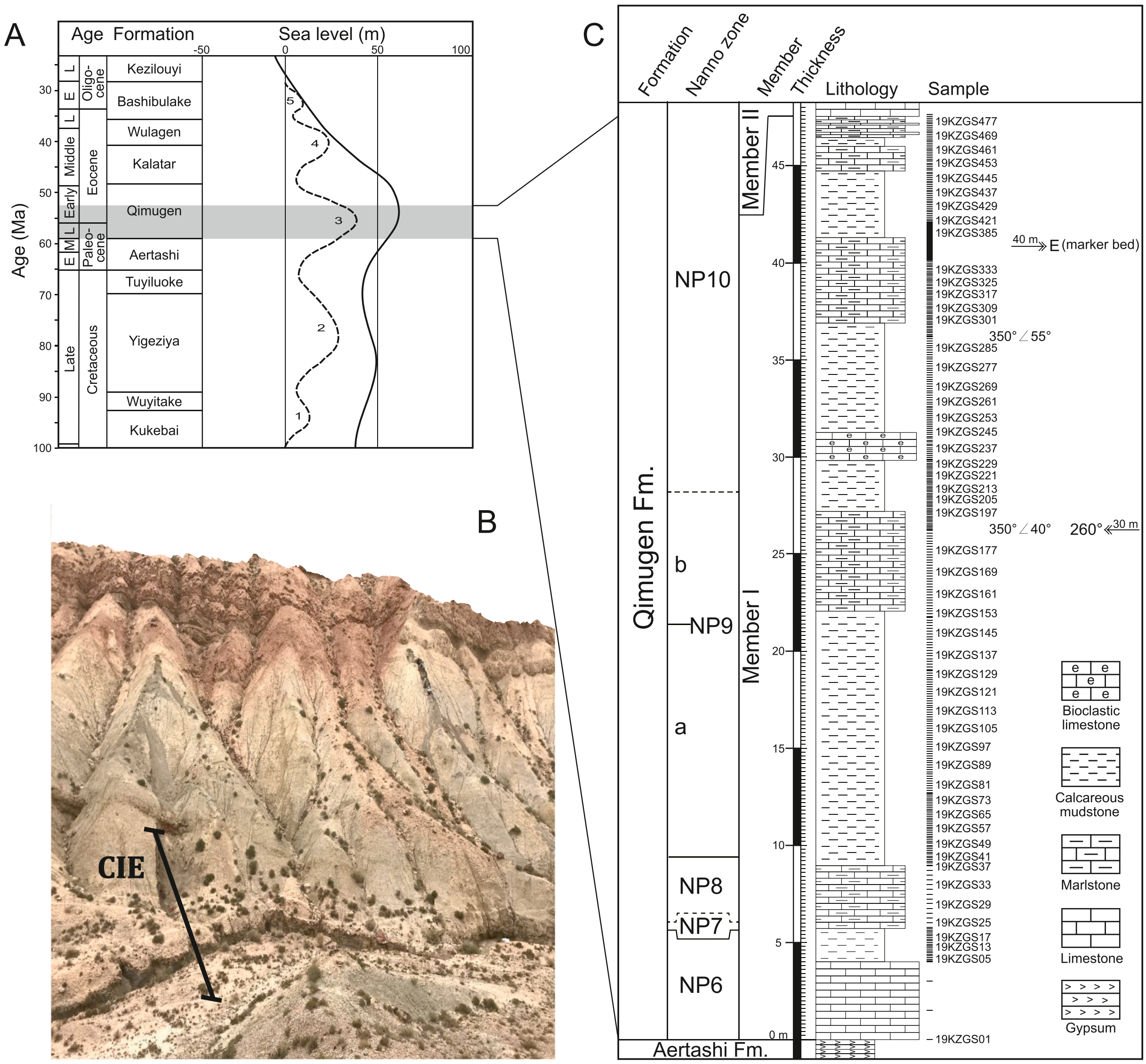

Fig. 2. A) Schematic regional stratigraphy and sea level change in the Tarim Basin (Bosboom et al., 2011, 2014); B) Outcrop of the Kuzigongsu section showing the approximate extended range of the CIE; C) Lithologic column of the sampled section.

shallow water carbonate platform as documented by the Qimugen Formation in the southwestern Tarim Basin (Fig. 2; Li et al., 2021).

2.2. Regional geography and lithology of the sampled section

The Kuzigongsu section (39°44′19“ N, 75°18′20” E) is located 5 km NW of the Wuqia County, bordering the northwestern Kashgar of China and Kyrgyzstan (Fig. 1). The study section was originally deposited along an east-facing terrigenous-rich foreland basin referred to as the "Tarim Sea", which was connected to the Siberian Sea to the north (Lippert et al., 2014; Jiang et al., 2018). This section is adjacent to several small gypsum mine fields in the Paleocene Aertashi Formation. The Aertashi, Qimugen, and Kalatar formations are continuously exposed along the slopes due to limited vegetation cover (Fig. 2), offering easy access to the sampled section. The Kuzigongsu section is 47.6 m thick and spans the lower part of the Qimugen Formation. It consists primarily of limestone, marlstone (or calcareous mudstone), and bivalve-rich limestone. The basal section is a 4 m-thick grey massive limestone overlain by alternating grayish-green calcareous mudstone and grey marlstone in the middle and a massive limestone on the top (Fig. 2).

3. Materials and methods

3.1. Calcareous nannofossil biostratigraphy

A total of 123 samples were selected for calcareous nannofossil analysis. The top >1 m of surface weathered rocks were removed and fresh rock chips were carefully collected to avoid weathering contamination. Average sample spacing was approximately 0.4 m, which is equivalent to ~16 kyr intervals. The central portion of freshly broken rock pieces without cracks was taken to prepare smear slides for calcareous nannofossil analysis. The smear slides were prepared using the standard technique to avoid assemblage differentiation (Bown, 1998). Slides were mounted with Norland Optical Adhesive No. 61, cured under UV light and examined with a Zeiss Axio ImagerA2 light microscope under cross-polarized and plane-transmitted light at 1000× magnification. Micrographs were taken with a Zeiss Axiocam 506 color 6-megapixel digital camera.

Calcareous nannofossil taxonomy was determined following the concepts of Perch-Nielsen (1985) and Bown (1998), and the biozonation of Martini (1971) was used, supplemented by the zonation of Agnini et al. (2014). An initial semiquantitative analysis was conducted to determine species abundance and to identify rare taxa. Additional scanning provided a more precise biostratigraphic determination. Only the top and/or bottom of a continuous occurrence of a marker species was used to define the corresponding datum, and consideration was given to barren intervals when defining the continuity of occurrence. The sporadic presence of a marker species above the datum was considered to be reworked. Each nannofossil datum was assigned an orbitally tuned age of Gradstein et al. (2012) to roughly estimate linear compacted sedimentation rates.

3.2. Geochemical analyses

Planktonic and benthic foraminifers are sparse and poorly preserved due to compaction and lithification, consistent with a previous study at the nearby Bashibulake section (Jiang et al., 2018), and therefore geochemical analyses on whole rock samples were conducted in this study.

The fresh rock samples were ground and homogenized with an agate mortar and pestle to obtain a powder which could pass through a 200-mesh (75 μm) sieve. About 0.8 g of the powder was weighed and pressed into a disc using a tablet-making machine for X-Ray Fluorescence (XRF) analysis (Model FW-5 Powder-to-tablet Machine, China) under a pressure of 20 MPa. The elemental composition of each tablet was measured 10 times with an EDX-6000B X-ray fluorescence spectrometer (XRF; Skyray Instrument Inc., China), and the average was calibrated with a Chinese national stream sediment standard (GBW07305a). The variance was better than 5% for the major oxides (P_2O_5, TiO_2, SiO_2, Al_2O_3, Fe_2O_3, MgO, CaO, K_2O) and 10% for the minor elements, based on the repeated measurements of the standard processed with each batch of samples.

Another aliquot of the powder was weighed for bulk carbonate carbon and oxygen isotopic analysis. No pretreatment was used in order to avoid potential carbon isotopic exchange between calcium carbonate and organic matter (Wierzbowski, 2007). The subsample was reacted with 100% phosphoric acid at 72 °C and the carbon and oxygen isotopic ratios of the CO_2 produced were analyzed using a Gas Bench II Auto-Carbonate device connected to a Thermo Finnigan Delta Plus Advantage mass spectrometer at the Key Laboratory of Submarine Geosciences of the Second Institute of Oceanography, Ministry of Natural Resources, China. The isotopic data were calibrated based on measurements of an international standard (NBS-19) and two Chinese National Standards (GBW04405 and GBW04406) analyzed with each batch of samples. Isotopic results are reported in the standard delta notation as $\delta^{13}C_{carb}$ and $\delta^{18}O_{carb}$ in reference to the international Vienna Pee Dee Belemnite (VPDB) standard. Analytical precision is better than 0.1‰ for $\delta^{13}C_{carb}$ and 0.2‰ for $\delta^{18}O_{carb}$ based on replicate analyses of the standards processed with each batch of samples.

Weight percent $CaCO_3$ (wt% $CaCO_3$) was measured using a modified acid soluble weight-loss method (Molnia, 1974), which was improved over the standard method and minimizes the errors by (1) using the XRF CaO data as a first-order estimate of the HCl to be added; (2) lengthening reaction time to overnight in a 40 °C bath; (3) decanting supernatant after lengthened centrifuging during the rinsing process with deionized distilled water until the pH was ~7; and (4) using multiple carbonate standards to calibrate as an integral part of the analysis. The advantage over other methods is that the resulting residue can be used for further total organic carbon (TOC) and stable C and N isotopic analyses. The analytical error was better than 0.1% based on the five replicate measurements of an in-house carbonate standard (wt% $CaCO_3$ = 50%) run with each batch of samples.

4. Results

4.1. Calcareous nannofossil assemblages and biostratigraphy

Calcareous nannofossils are moderately preserved throughout the studied section with various degrees of overgrowth, fragmentation, and dissolution (Figs. 3-5; Supplementary Table S1). Most *Rhomboaster* specimens were unidentifiable due to heavy overgrowth or recrystallization (Fig. 5), the latter may be responsible for the formation of many siderite rhombohedrons seen in the Maryland South Dover Bridge (SDB) cores (Self-Trail et al., 2017) and the Kuzigongsu section (Supplementary Fig. S2). Fragmentation was commonly seen in *Micrantholithus* and *Discoaster* specimens, for which dissolution influenced the fragile central structures of *Toweius*, *Neochiastozygus*, and *Chiasmolithus*. Despite these diagenetic effects, most specimens were identifiable at the species level.

Most samples contain variable abundances of nannofossils except for those from intervals corresponding to the onset of the carbon isotope excursion (Fig. 3; Supplementary Table S1), with high abundances occurring below the lowermost 10 m and above the PETM recovery (the uppermost 15 m). A total of 73 species belonging to 33 genera were observed (Figs. 4 and 5). The dominant taxa include, in descending order, *Coccolithus pelagicus*, *Toweius pertusus*, *T. eminens*, *T. callosus*, *Pontosphaera exilis*, *Micrantholithus flos*, *T. rotundus*, *Discoaster multiradiatus*, and *Neochiastozygus junctus*. The maximum absolute abundance reached 1553 individuals/100 field of views (FOVs) at 7.0 m, and *C. pelagicus*, *T. pertusus* and *T. eminens* dominated the assemblage with an average relative abundance of 61.6%. The pre-PETM interval contains mostly *C. pelagicus* and various species of *Prinsius*, *Toweius*, *Heliolithus*, *Fasciculithus*, and *Chiasmolithus*. Various *Discoaster* species occur above 10 m and co-dominate the pre-PETM nannofossil assemblages with *C. pelagicus*. The PETM interval is characterized by the presence of the distinct *Rhomboaster* spp.–*Disocaster araneus* (RD) association, *Coccolithus bownii*, and *Discoaster acutus*. The absolute abundance of calcareous nannofossils during the PETM is extremely low, with an average of 167 specimens/100 FOVs. The percent abundance of *Micrantholithus astrum* and *M. flos* increased during the PETM, with average values increasing from 0.2% and 1.5% in the pre-CIE to 2.4% and 4.6% during the PETM, respectively. In addition, the percent abundance of *Neochiastozygus junctus* also increased rapidly during the PETM interval from 0.9% to 5.4%, while *T. pertusus* and *T. eminens* decreased significantly from 20.5% and 8.0% to 13.0% and 3.3%, respectively. The post-CIE assemblages contain dominant nannofossil taxa that are similar to those of the pre-CIE except without *Fasciculithus* and *Prinsius* but with *Discoaster*.

A continuous sequence of nannofossil Zones NP6 through NP10 was recognized according to the stratigraphically ordered occurrence of zonal markers, and additional datums are consistent with the zonal boundaries (Fig. 3; Supplementary Table S2). From bottom to top, the first occurrence (FO) of *Heliolithus kleinpellii* defines the base of Zone NP6, the FO of *Heliolithus riedelii* defines the NP7/NP8 boundary, the FO of *Discoaster multiradiatus* defines the zone NP9, and the subzone NP9b/NP9a boundary was placed at FO of the "excursion taxa" *D. araneus*. The base of Zone NP10 was identified by the FO of *Rhomboaster bramlettei*.

4.2. Bulk carbonate $\delta^{13}C_{carb}$ and $\delta^{18}O_{carb}$

The most prominent characteristic of the PETM at this site is the negative excursions in both the carbon and oxygen isotopes. As shown in Figs. 6 and 7, the measured bulk carbonate $\delta^{13}C_{carb}$ values at the Kuzigongsu section fall between −5.2‰ and 4.7‰, and $\delta^{18}O_{carb}$ values between −8.3‰ and 0.5‰. Both $\delta^{13}C_{carb}$ and $\delta^{18}O_{carb}$ values show an abrupt negative shift at 19.9 m and a rapid recovery at 30.5 m (Supplementary Table S2). In addition, four gaps in the bulk carbonate record occur within the CIE due to the lack of calcareous materials. The post-PETM $\delta^{13}C_{carb}$ and $\delta^{18}O_{carb}$ values do not recover to pre-PETM values and level out upsection.

Based on the abruptness of changes in bulk-carbonate carbon isotopes, we divided the studied section into pre-PETM (0–19.9 m), PETM (19.9–30.5 m) and post-PETM (30.5–47.6 m) intervals. The PETM interval (19.9–30.5 m) was further subdivided into the CIE onset (19.9–20.6 m), CIE body (20.6–29.8 m), and CIE recovery (29.8–30.5 m) according to the definitions by Röhl et al. (2007).

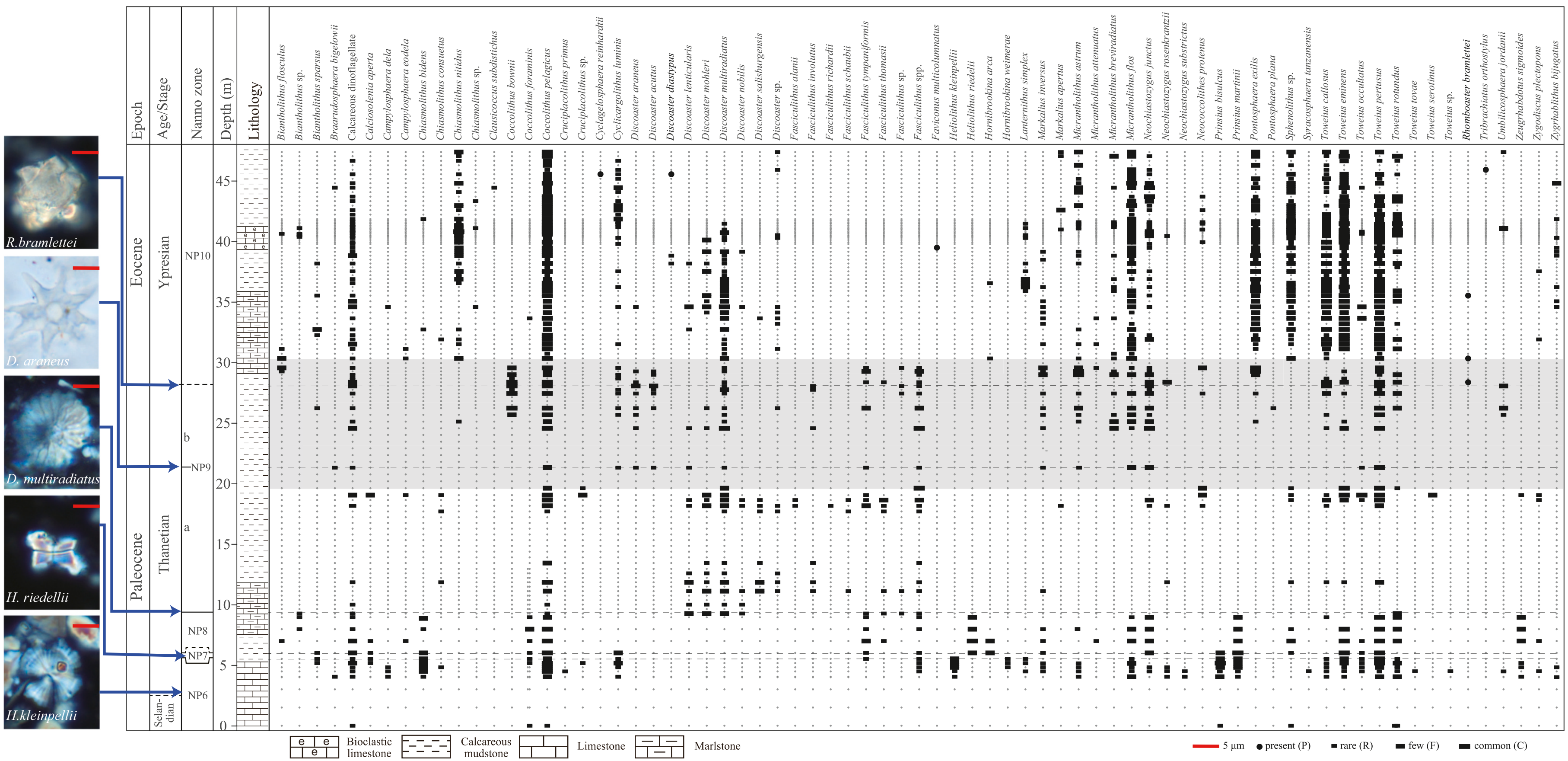

Fig. 3. Calcareous nannofossil distribution in the Kuzigongsu section, Tarim Basin (NW China).

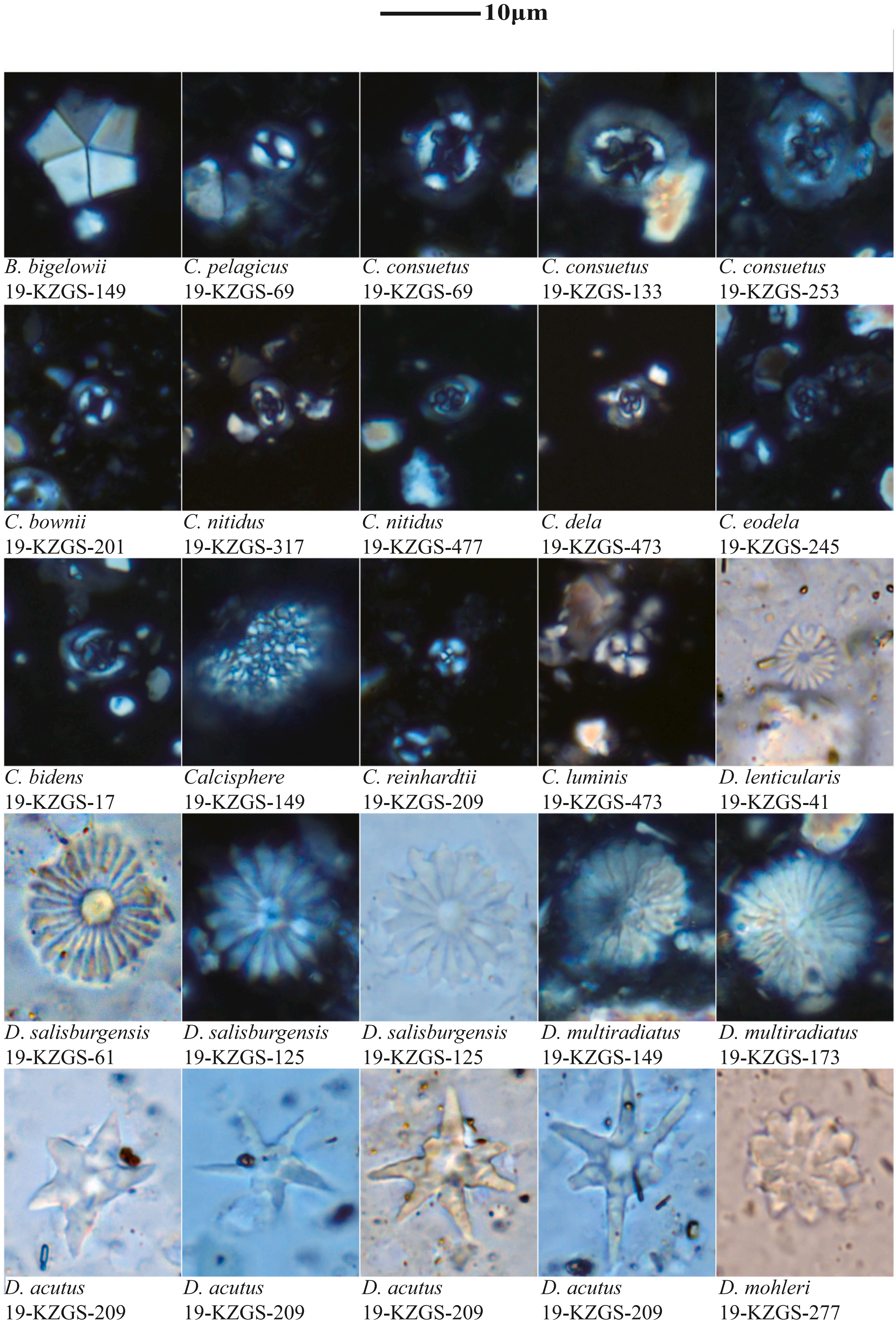

Fig. 4. Selected calcareous nannofossils observed in the Kuzigongsu section, Tarim Basin (NW China). Sample positions are shown in Fig. 1.

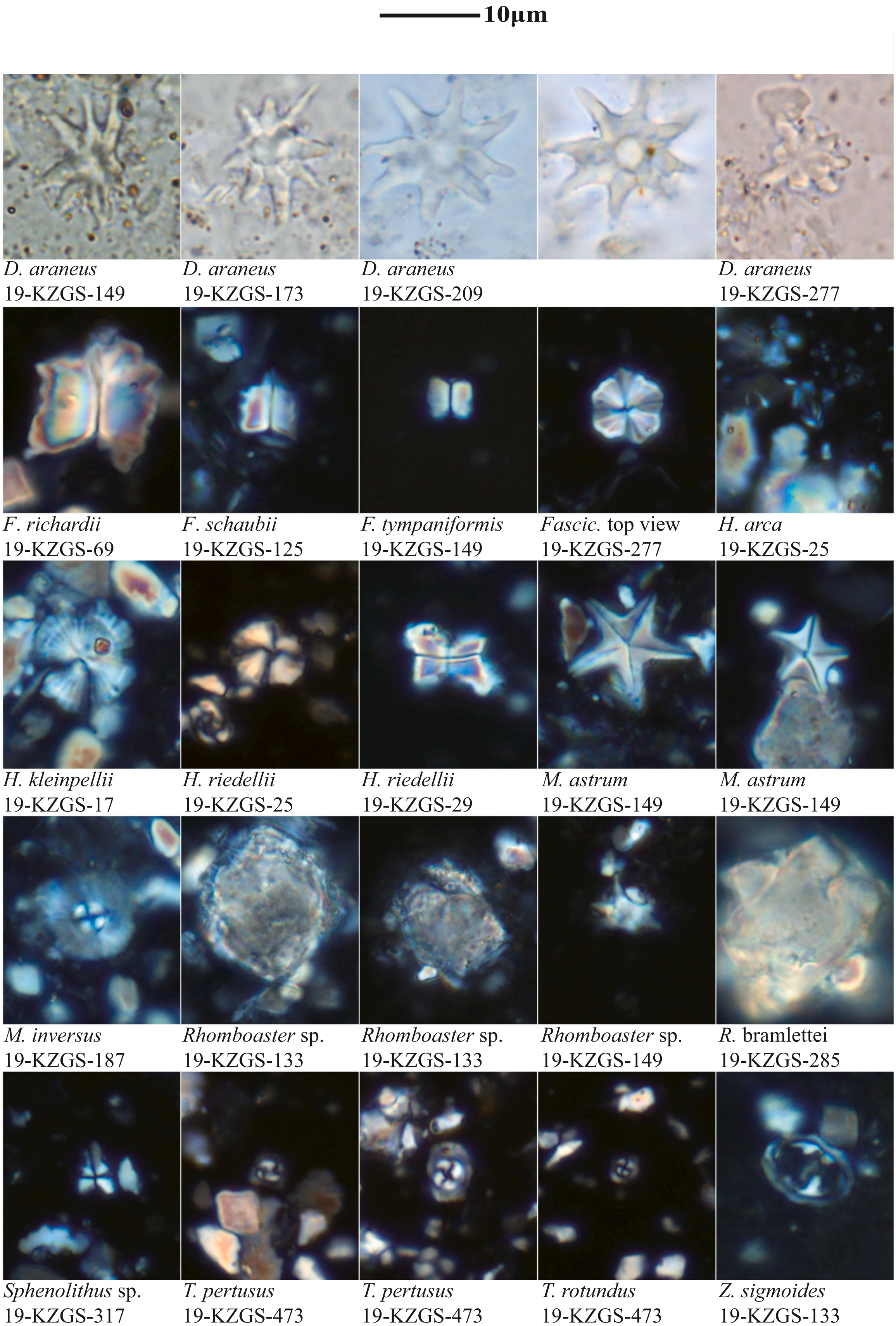

Fig. 5. Selected calcareous nannofossils observed in the Kuzigongsu section, Tarim Basin (NW China). Location of sample numbers are shown in Fig. 1.

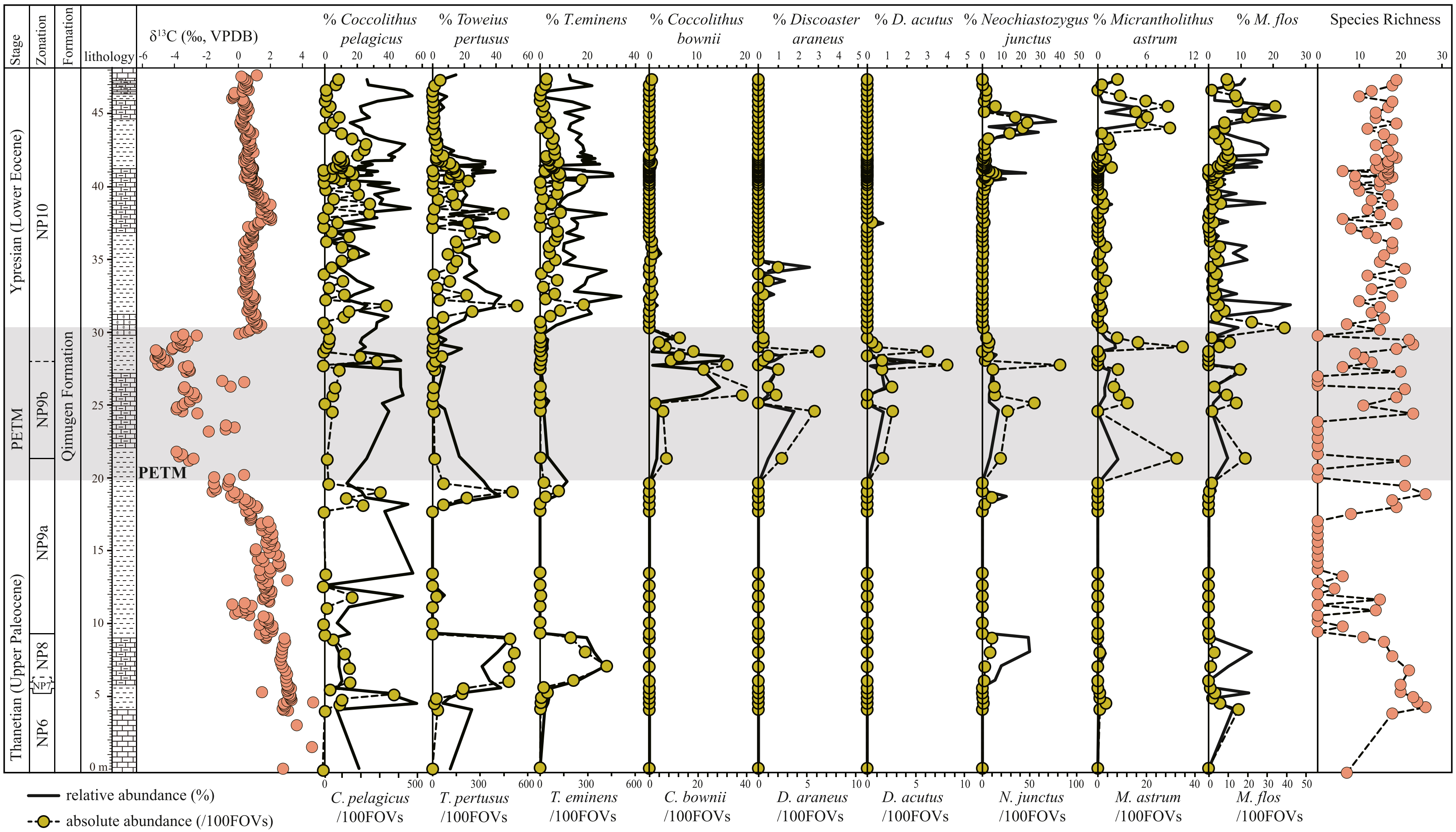

Fig. 6. Variation in selected calcareous nannofossil species across the PETM at the Kuzigongsu section, Tarim Basin (NW China). Solid line denotes percentage abundance, and dashed line indicates absolute abundance (number of specimens encountered in 100 FOVs).

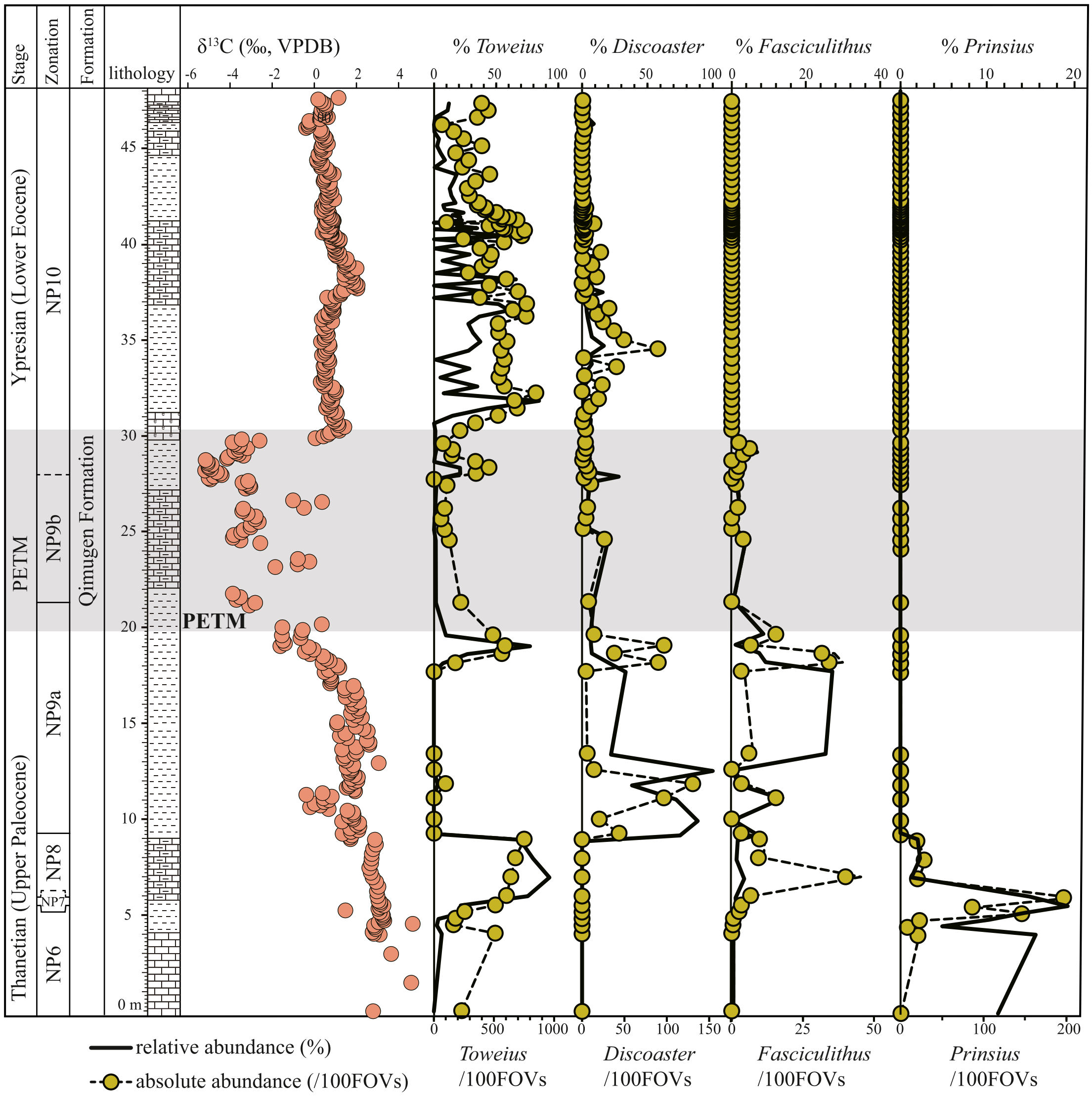

Fig. 7. Variation in genera *Toweius*, *Discoaster*, *Fasciculithus* and *Prinsius* across the PETM at the Kuzigongsu section, Tarim Basin (NW China). Solid line denotes percentage abundance, and dashed line indicates absolute abundance (number of specimens encountered in 100 FOVs).

4.3. Major and trace element geochemistry based on XRF

Both major and trace elements show significant variation across the PETM and are reported according to their paleoenvironmental indications: (1) proxies for nutrient condition such as P and Zn/Al, with higher values indicating higher nutrient supply (Khozyem et al., 2013); (2) proxies for detrital input and weathering intensity such as Ti/Al and K/Al, with higher values indicating enhanced delivery of detrital materials from various sources (Bertrand et al., 1996; Murphy et al., 2000).

In general, various proxies in each group show a similar trend (Fig. 7). Phosphorus concentrations and nutrients-related elemental ratios are high in the lower 10 m of section, decrease abruptly up section before the PETM (P: 9.0 m; Zn/Al: 4 m) and increase evidently during the PETM interval, and then level out during the post-PETM interval. Weathering proxies show an increasing trend below 10 m (with K/Al displaying a gradual increase and Ti/Al an abrupt shift at 9 m), remain high from 10 m and throughout the PETM where several negative shifts occur, decrease abruptly at the end of PETM recovery phase (30.5 m), followed by a brief increase and then level off during the post-PETM interval.

5. Discussion

5.1. The shallow marine PETM record at the Kuzigongsu section in the Paratethys

The PETM at the Kuzigongsu section was identified based on a negative excursion in bulk $\delta^{13}C_{carb}$ and $\delta^{18}O_{carb}$ (about 6.3‰ and 4.5‰, respectively), presence of calcareous nannofossil Zones NP9 and NP10, and an abrupt color change of the shale from greenish to black. The calcareous nannofossil "excursion taxa" *Coccolithus bownii, Discoaster araneus*, *D. acutus*, *Rhomboaster bramlettei* (Figs. 4 and 5) are typically restricted stratigraphically to the PETM interval and are often used to identify the event (Kahn and Aubry, 2004; Self-Trail et al., 2012; Bralower and Self-Trail, 2016). The stratigraphic distribution of the "excursion taxa" at the Kuzigongsu section falls within 19.9–30.5 m, and is consistent with the range of negative excursion in $\delta^{13}C_{carb}$ and $\delta^{18}O_{carb}$ (Figs. 6 and 7). Moreover, the completeness of the section is indicated by the successive occurrence of the eight nannofossil datums recognized (Supplementary Table 1, Fig. S1). Our newly reported PETM record is associated with a much higher sampling resolution than the previously published shallow marine records in the Tarim region (Li et al., 2017; Zhang et al., 2017; Cao et al., 2018; Li et al., 2021), and does not have any obvious truncation or condensation as evidenced by field observation and biostratigraphy (detailed below). The presence of a complete, shallow-water PETM record at the Kuzigongsu section fills a major data gap in the Paratethys, a key region needed to understand the trigger and recovery mechanisms of the PETM (Kennett and Stott, 1991; Zhu et al., 2019).

As Walther's Law states, any vertical progression of facies is the result of a succession of depositional environments that are laterally juxtaposed to each other (López, 2015). As shown in the stratigraphic column (Fig. 2), the Kuzigongsu section spans the lower Qimugen Formation marlstones and calcareous mudstones and is sandwiched between the massive Aertashi gypsum beds at the base and the upper Qimugen brown gypsum-bearing mudstones on the top. Such a temporal superposition of lithology constrains the Kuzigongsu section to a shallow marine depositional environment according to the Walther's Law, as gypsum deposits characterize shallow evaporative environments (Hardie and Eugster, 1971). As depositional environments change their lateral position due to transgression and regression, the sedimentary facies of adjacent depositional environments will overlap one another as a vertical sequence. Therefore, the vertical sequence of facies mirrors the original lateral distribution of sedimentary environments. The presence of marlstone and gypsum, along with the red color on the top of the Kuzigongsu section, suggests a tidal flat environment for the underlying and overlying sediments of the Kuzigongsu section (Reif and Slatt, 1979).

Nannofossil species *Micrantholithus astrum* and *M. flos* are indicators of shallow epicontinental sea environment (Bown, 2005; Bartol et al., 2008). Their common occurrence at the Kuzigongsu section (Fig. 5) suggests that the Paratethys in the southwestern Tarim Basin was a shallow marine environment during the PETM. These two characteristic species are also common in the nearby Bashibulake Section (Cao et al., 2018), supporting this part of the Tarim Basin was a shallow marine environment during the PETM. This is consistent with the inference from calcareous nannofossils, foraminifera and microfacies analysis from other nearby sections in southwestern Tarim Basin (Cao et al., 2018; Jiang et al., 2018; Zhang et al., 2018; Li et al., 2021). More specifically, the Paratethys Seaway in the southwestern Tarim Basin was a carbonate platform environment based on microfacies analysis of Li et al. (2021), which shows predominantly marlstones with abundant bioclasts such as foraminifers, bivalves and serpulids. In contrast, pentaliths, such as *Micrantholithus astrum* and *M. flos*, are very rare in the mid-Atlantic Coastal Plain (Self-Trail et al., 2012), likely reflecting regional oceanographic heterogeneity across the PETM. The better preservation of calcareous nannofossil assemblages in the mid-Atlantic Coastal Plain may be attributed to its drill core rather than outcrop samples and its higher sedimentation rates (Self-Trail et al., 2012), which can result in rapid burial and thereby improve the preservation of calcareous nannofossils.

5.2. Calcareous nannoplankton responses to the PETM

Calcareous nannoplankton responses to the rapid and extreme warming conditions during the PETM have been documented at a variety of deep-ocean settings (Bralower, 2002; Kahn and Aubry, 2004; Gibbs et al., 2006a; Jiang and Wise Jr., 2006; Angori et al., 2007; Mutterlose et al., 2007) and coastal and continental margin regions (Agnini et al., 2007; Angori et al., 2007; Bown and Pearson, 2009; Self-Trail et al., 2012; Bralower and Self-Trail, 2016). The quantitative analyses of calcareous nannofossil assemblage compositions suggest that the biological productivity increased in coastal and continental margin regions but decreased in the open ocean during the PETM (Gibbs et al., 2018).

Changes in calcareous nannofossil assemblages combined with geochemical proxies can be used to assess the surface water productivity in the Paratethys during the PETM. *Neochiastozygus junctus* is thought to represent mesotrophic to eutrophic conditions and to have flourished in high productivity environment of the New Jersey and Maryland shelves (Fig. 9; Gibbs et al., 2006b; Self-Trail et al., 2012). As a result, *N. junctus* is commonly used as a proxy for surface ocean primary productivity. The relative abundance of *N. junctus* increases dramatically from a pre-PETM average of 0.9% to 5.4% during the PETM at the Kuzigongsu section (Fig. 6), suggesting that the primary productivity in the Paratethys increased during the PETM.

The inferred increase in productivity based on increased abundance of *N. junctus* is consistent with the productivity proxies based on geochemical data. It has been suggested that the phosphorus concentration and Zn/Al values can be used as nutrient indicators because both phosphorus and zinc are essential elements for marine organisms and are productivity sensitive (Khozyem et al., 2013). An increase in both P and Zn/Al at ~20 m is supportive of increased nutrient condition and elevated primary productivity across the PETM (Fig. 8). The increased nutrient condition may be facilitated by enhanced continental weathering, as evidenced by higher values of Ti/Al and K/Al ratios (Fig. 8), which are commonly used as weathering proxies (Bertrand et al., 1996; Murphy et al., 2000). It is plausible that the warmer climate during the PETM led to increased weathering intensity, which allowed the transport of terrestrially derived nutrients into the Paratethys, promoting marine productivity (Fig. 9.).

5.3. Shallow ocean acidification in the Paratethys during the PETM

Ocean acidification has been inferred based on decreased ocean pH based on boron isotope and B/Ca proxies and significant carbonate dissolution observed in the deep sea (e.g., Babila et al., 2016; Babila et al., 2018; Penman et al., 2014; Zachos et al., 2005), but the excellent preservation of foraminifera and the lack of severe benthic extinction in the mid-Atlantic Coastal Plain during the PETM argue against extreme ocean acidification in shelf settings (Stassen et al., 2012). This is because continental shelf environments are affected by complex processes related to terrestrial input, coastal upwelling, and mixing of the water mass (Self-Trail et al., 2012; Stassen et al., 2013; Bralower et al., 2018). Some suggest that shelf acidification occurred in the eastern US/mid-Atlantic coastal plain based on B/Ca in planktonic foraminifera during the low carbonate intervals in the Maryland-New Jersey depth transect during the main phase of the PETM (Babila et al., 2016), and the reduced carbonate intervals suggest a shoaling of the calcite compensation depth and the lysocline to the middle shelf (120–130 m; Bralower et al., 2018). Following the CO_2 emissions, continental weathering delivering alkalinity input possibly may have helped neutralize the ocean pH and buffer changes in ocean acidity in coastal waters. This not only helps minimize the extinction of benthic foraminifera along the shelf (Babila et al., 2016), but increase the survival of pteropods through the water column (Janssen et al., 2016).

Surface ocean acidification in the Paratethys can be inferred by paleontological and geochemical indicators such as changes in the abundance, morphology, preservation state and composition of calcareous organisms, and wt% $CaCO_3$. The wt% $CaCO_3$ at the Kuzigongsu section is near 100% in the lowermost part of the section, rapidly decreasing upsection and reaching near zero values during the PETM interval, and rebounding to high levels after the PETM (Fig. 8). Additionally, the absolute abundance of calcareous nannofossils decreased sharply during the PETM interval, with an average of only 167 individuals per 100 view fields (Fig. 8). The whole shield index (WSI; see Bralower et al., 2018) abruptly increased during the PETM, indicating a deterioration in the preservation state of calcareous nannofossils due to the dissolution of fragile structures.

As a vast epicontinental sea surrounded by the Eurasian continents (Mao and Norris, 1984; Tang, 1992; Bosboom et al., 2011), the Paratethys has been shown to respond in more complex ways due to environmental heterogeneity and intense land-sea interactions (Afzal et al., 2011; Stassen et al., 2013; Li et al., 2017; Self-Trail et al., 2017; Bralower et al., 2018; Ivany et al., 2018; Zhang et al., 2019). Sedimentary wt% $CaCO_3$ depends on the carbonate production in the surface ocean, the

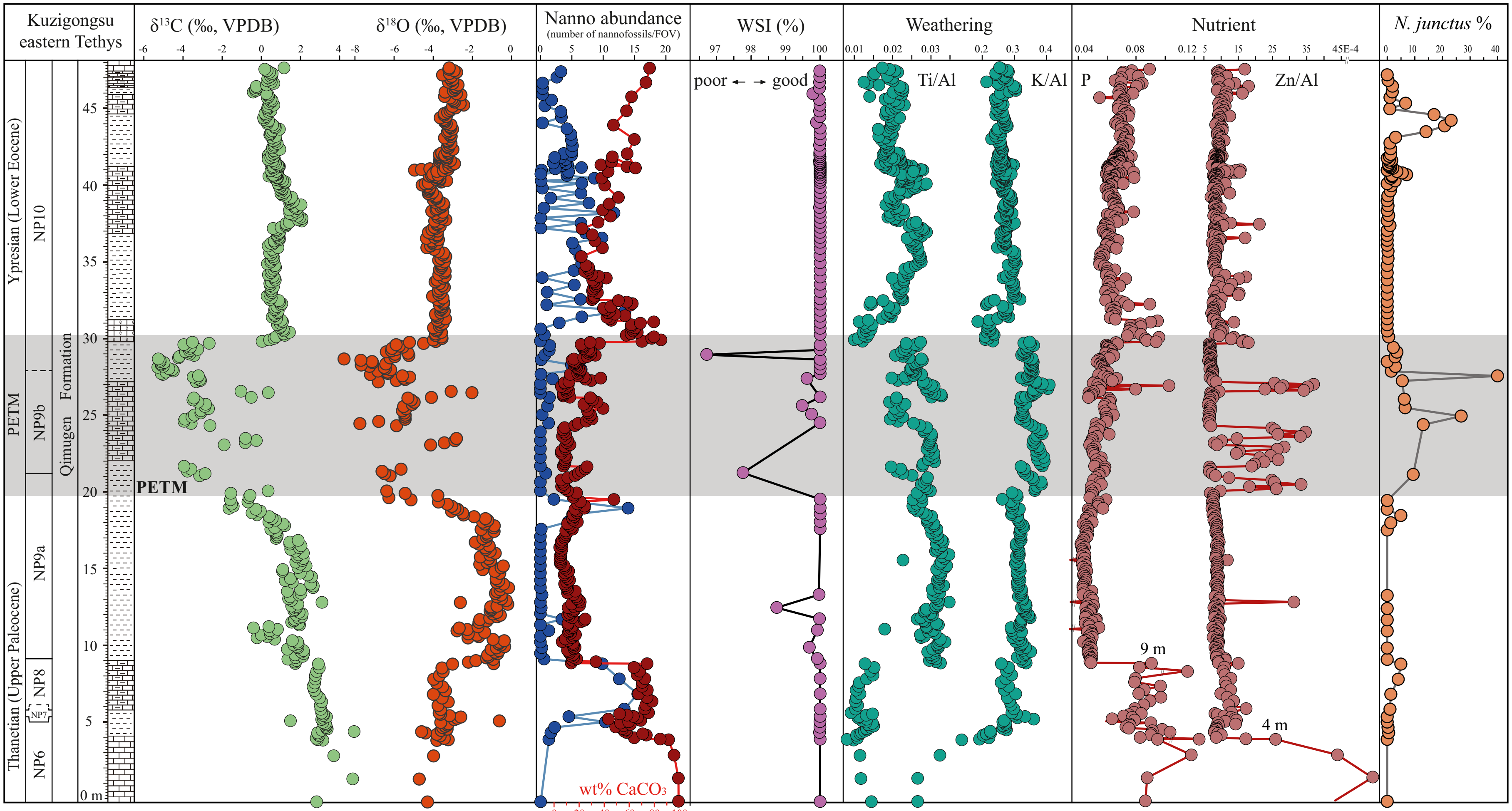

Fig. 8. Variation in biological and geochemical proxies across the PETM at the Kuzigongsu section, Tarim Basin (NW China). WSI is the whole shield index (after Bralower et al., 2018).

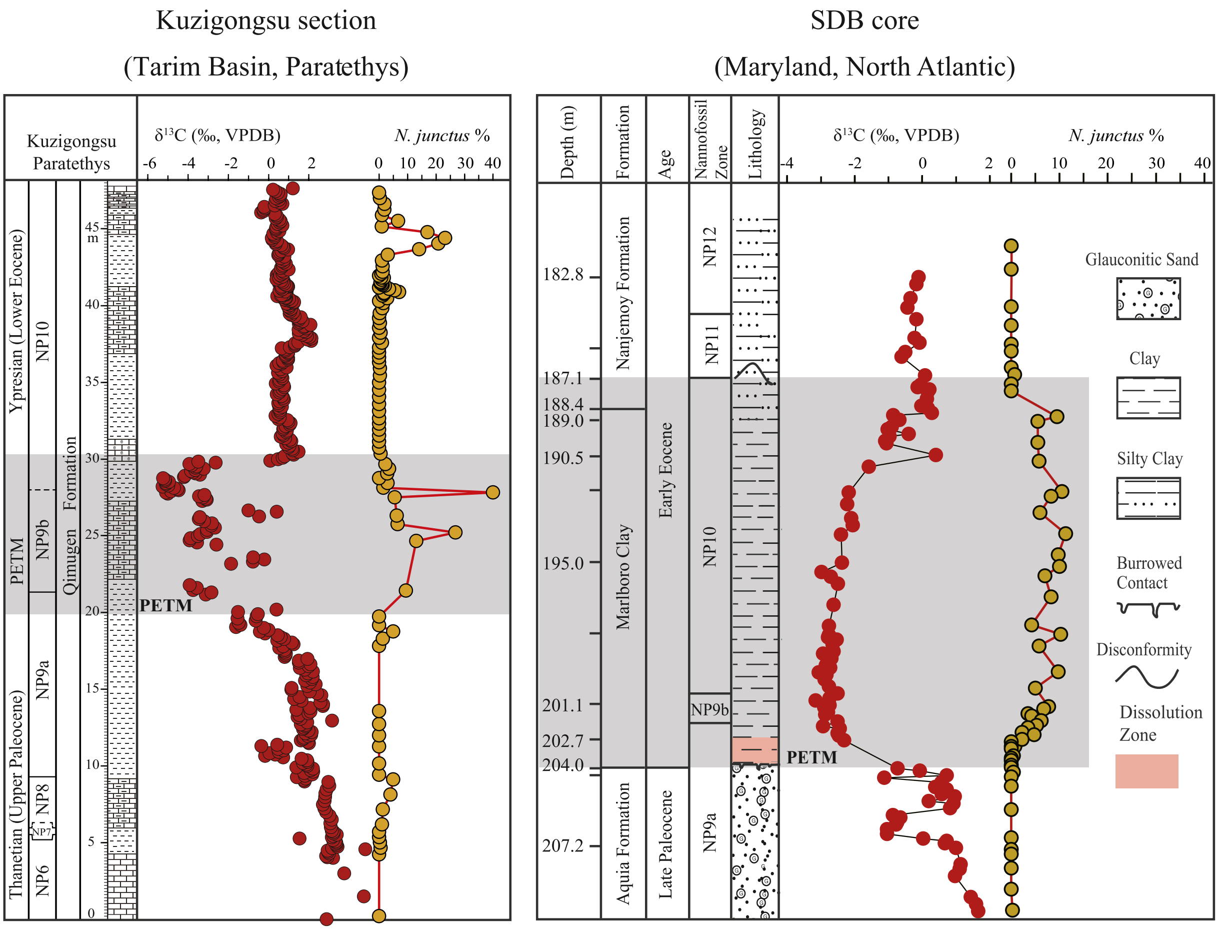

Fig. 9. Productivity comparison between the Kuzigongsu section (Tarim Basin, NW China) and the South Dover Bridge (SDB) core, mid-Atlantic Coastal Plain, USA. SDB Data from Self-Trail et al. (2012)

dissolution in the water column, and the dilution by non-carbonate materials (Berger, 1992). These three separated processes could contribute to the highly fluctuated wt% $CaCO_3$ at the Kuzigongsu section.

Ocean acidification may have occurred in the shallow seawaters of the Paratethys during the PETM based on the poor preservation (lower WSI values; Fig. 8) and many barren samples of calcareous nannofossils, and the near zero wt% $CaCO_3$ values within the PETM interval (19.9–25.0 m). However, additional mechanisms other than dissolution are needed to explain the comparable lows in wt% $CaCO_3$ and nannofossil abundance in the pre-PETM interval (8.0–18.0 m; Fig. 8). The remarkable increase in Ti/Al and K/Al ratios at 4.0 m, 9.0 m and 19.9 m is coincident with the abrupt decline in wt% $CaCO_3$ and nannofossil abundance, suggesting that enhanced weathering intensity, and thus stronger dilution influence is possible during the pre- and *syn*-PETM intervals. In addition, freshening of the surface ocean due to increase in precipitation may have also contributed to the decrease in wt% $CaCO_3$ in the Paratethys, because calcareous nannofossils and planktonic foraminifera are unable to tolerate the less saline conditions (Self-Trail et al., 2017), resulting in decreased abundance of calcareous plankton and calcium carbonate production. Therefore, it seems ocean acidification, terrestrial dilution, and reduced carbonate production due to surface ocean freshening have jointly contributed to the large fluctuation in wt% $CaCO_3$ and calcareous nannofossil abundance observed in the Kuzigongsu section.

6. Conclusions

A detailed analysis of calcareous nannofossils in the Kuzigongsu section allows for the establishment of a high-resolution biostratigraphic framework for the upper Paleocene through lower Eocene of the Tarim Basin in the Paratethys. The consistent stratigraphic range of “excursion taxa” suggests that they are good micropaleontological markers for identifying PETM records in the Paratethys. The common occurrence of nearshore taxon *Micrantholithus* suggests a middle to outer neritic depositional setting for the Kuzigongsu section. The significant increase in the relative abundance of the high-productivity taxon *N. junctus* coincides with higher values of nutrient and weathering proxies, indicating that the PETM warming may have enhanced continental weathering and increased nutrient input through runoff into the basin, promoting marine primary productivity. The decrease in wt% $CaCO_3$ values suggests that ocean acidification may have occurred in the shallow water of the Paratethys.

Declaration of Competing Interest

The authors declare no competing interests.

Data availability

Data in Brief

Acknowledgments

We sincerely thank Yanggang Gu (South China Sea Fisheries Research Institute, China) for field sample collection. Insightful critics and suggestions from two anonymous reviewers greatly improved the earlier version of this paper. This research is financially supported by the NSFC grants 41888101 & 41976045 and the Innovation Group Project of Southern Marine Science and Engineering Guangdong Laboratory (Zhuhai) (No. 311021002) to S.J., and the NSF Award 2002370 to Y.C.

Appendix A. Supplementary data

Supplementary data to this article can be found online at https://doi.org/10.1016/j.gloplacha.2022.103918.

References

Afzal, J., Williams, M., Leng, M.J., Aldridge, R.J., 2011. Dynamic response of the shallow marine benthic ecosystem to regional and pan-Tethyan environmental change at the Paleocene-Eocene boundary. Palaeogeogr. Palaeoclimatol. Palaeoecol. 309 (3–4), 141–160.

Agnini, C., Fornaciari, E., Rio, D., Tateo, F., Backman, J., Giusberti, L., 2007. Responses of calcareous nannofossil assemblages, mineralogy and geochemistry to the environmental perturbations across the Paleocene/Eocene boundary in the Venetian Pre-Alps. Mar. Micropaleontol. 63 (1–2), 19–38.

Agnini, C., Fornaciari, E., Raffi, I., Catanzariti, R., Palike, H., Backman, J., Rio, D., 2014. Biozonation and biochronology of Paleogene calcareous nannofossils from low and middle latitudes. Newsl. Stratigr. 47 (2), 131–181.

Alegret, L., Ortiz, S., Orue-Etxebarria, X., Bernaola, G., Baceta, J.I., Monechi, S., Apellaniz, E., Pujalte, V., 2009. The Paleocene–Eocene thermal maximum: new data on microfossil turnover at the Zumaia section, Spain. PALAIOS 24 (5), 318–328.

Angori, E., Bernaola, G., Monechi, S., 2007. Calcareous nannofossil assemblages and their response to the Paleocene-Eocene thermal maximum event at different latitudes; ODP Site 690 and Tethyan sections. Special Paper - Geological Society of America 424, 69–85.

Babila, T.L., Rosenthal, Y., Wright, J.D., Miller, K.G., 2016. A continental shelf perspective of ocean acidification and temperature evolution during the Paleocene-Eocene Thermal Maximum. Geology 44 (4), 275–278.

Babila, T.L., Penman, D.E., Hönisch, B., Kelly, D.C., Bralower, T.J., Rosenthal, Y., Zachos, J.C., 2018. Capturing the global signature of surface ocean acidification during the Palaeocene–Eocene Thermal Maximum. Philos. Trans. R. Soc. A Math. Phys. Eng. Sci. 376 (2130), 20170072.

Bartol, M., Pavšič, J., Dobnikar, M., Bernasconi, S.M., 2008. Unusual Braarudosphaera bigelowii and Micrantholithus vesper enrichment in the early Miocene sediments from the Slovenian Corridor, a seaway linking the Central Paratethys and the Mediterranean. Palaeogeogr. Palaeoclimatol. Palaeoecol. 267 (1–2), 77–88.

Berger, W., 1992. Pacific carbonate cycles revisited: arguments for and against productivity control. In: Ishizaki, K., Saito, T. (Eds.), Centenary of Japanese Micropaleontology, pp. 15–25.

Bertrand, P., Shimmield, G., Martinez, P., Grousset, F., Jorissen, F., Paterne, M., Pujol, C., Bouloubassi, I., Menard, P.B., Peypouquet, J.P., Beaufort, L., Sicre, M.A., Lallier-Verges, E., Foster, J.M., Ternois, Y., 1996. The glacial ocean productivity hypothesis: the importance of regional temporal and spatial studies. Mar. Geol. 130 (1), 1–9.

Bosboom, R., Dupont-Nivet, G., Houben, A., Brinkhuis, H., Villa, G., Mandic, O., Stoica, M., Zachariasse, W., Guo, Z., Li, C., Krijgsman, W., 2011. Late Eocene Sea retreat from the Tarim Basin (west China) and concomitant Asian paleoenvironmental change. Palaeogeogr. Palaeoclimatol. Palaeoecol. 299 (3), 385–398.

Bosboom, R., Dupont-Nivet, G., Grothe, A., Brinkhuis, H., Villa, G., Mandic, O., Stoica, M., Kouwenhoven, T., Huang, W., Yang, W., Guo, Z., 2014. Timing, cause and impact of the late Eocene stepwise sea retreat from the Tarim Basin (west China). Palaeogeogr. Palaeoclimatol. Palaeoecol. 403, 101–118.

Bowen, G.J., Beerling, D.J., Koch, P.L., Zachos, J.C., Quattlebaum, T., 2004. A humid climate state during the Palaeocene/Eocene thermal Maximum. Nature 432 (7016), 495–499.

Bown, P.R., 1998. Calcareous Nannofossil Biostratigraphy. Kluwer Academic Publishers, Dordrecht, Netherlands, p. 314.

Bown, P.R., 2005. Palaeogene calcareous nannofossils from the Kilwa and Lindi areas of coastal Tanzania (Tanzania Drilling Project 2003-4). J. Nannoplankton Res. 27 (1), 21–95.

Bown, P.R., Pearson, P., 2009. Calcareous plankton evolution and the Paleocene/Eocene thermal maximum event: new evidence from Tanzania. Mar. Micropaleontol. 71 (1–2), 60–70.

Bralower, T.J., 2002. Evidence of surface water oligotrophy during the Paleocene-Eocene thermal maximum; nannofossil assemblage data from Ocean Drilling Program Site 690, Maud Rise, Weddell Sea. Paleoceanography 17 (2), 13.1-13.12.

Bralower, T.J., Self-Trail, J.M., 2016. Nannoplankton malformation during the Paleocene-Eocene Thermal Maximum and its paleoecological and paleoceanographic significance. Paleoceanography 31 (10), 1423–1439.

Bralower, T.J., Zachos, J.C., Thomas, E., Parrow, M., Paull, C.K., Kelly, D.C., Premoli Silva, I., Sliter, W.V., Lohmann, K.C., 1995. Late Paleocene to Eocene paleoceanography of the Equatorial Pacific Ocean; stable isotopes recorded at Ocean Drilling Program Site 865, Allison Guyot. Paleoceanography 10 (4), 841–865.

Bralower, T.J., Kump, L.R., Self-Trail, J.M., Robinson, M.M., Lyons, S., Babila, T., Ballaron, E., Freeman, K.H., Hajek, E., Rush, W., Zachos, J.C., 2018. Evidence for shelf acidification during the onset of the Paleocene-Eocene Thermal Maximum. Paleoceanogr. Paleoclimatol. 33.

Burtman, V.S., 2000. Cenozoic crustal shortening between the Pamir and Tien Shan and a reconstruction of the Pamir–Tien Shan transition zone for the Cretaceous and Palaeogene. Tectonophysics 319 (2), 69–92.

Cao, W., Xi, D., Melinte-Dobrinescu, M.C., Jiang, T., Wise, S.W., Wan, X., 2018. Calcareous nannofossil changes linked to climate deterioration during the Paleocene–Eocene thermal maximum in Tarim Basin, NW China. Geosci. Front. 9 (5), 1465–1478.

Carmichael, M.J., Inglis, G.N., Badger, M.P.S., Naafs, B.D.A., Behrooz, L., Remmelzwaal, S., Monteiro, F.M., Rohrssen, M., Farnsworth, A., Buss, H.L., Dickson, A.J., Valdes, P.J., Lunt, D.J., Pancost, R.D., 2017. Hydrological and associated biogeochemical consequences of rapid global warming during the Paleocene-Eocene Thermal Maximum. Glob. Planet. Chang. 157 (Supplement C), 114–138.

Carroll, A.R., Graham, S.A., Hendrix, M.S., Ying, D., Zhou, D., 1995. Late Paleozoic tectonic amalgamation of northwestern China: Sedimentary record of the northern Tarim, northwestern Turpan, and southern Junggar Basins. GSA Bull. 107 (5), 571–594.

Crouch, E.M., Dickens, G.R., Brinkhuis, H., Aubry, M.-P., Hollis, C.J., Rogers, K.M., Visscher, H., 2003. The Apectodinium acme and terrestrial discharge during the Paleocene-Eocene thermal maximum: new palynological, geochemical and calcareous nannoplankton observations at Tawanui, New Zealand. Palaeogeogr. Palaeoclimatol. Palaeoecol. 194 (4), 387–403.

Cui, Y., Kump, L.R., Ridgwell, A.J., Charles, A.J., Junium, C.K., Diefendorf, A.F., Freeman, K.H., Urban, N.M., Harding, I.C., 2011. Slow release of fossil carbon during the Palaeocene-Eocene Thermal Maximum. Nat. Geosci. 4 (7), 481–485.

Dickson, A.J., Rees-Owen, R.L., März, C., Coe, A.L., Cohen, A.S., Pancost, R.D., Taylor, K., Shcherbinina, E., 2014. The spread of marine anoxia on the northern Tethys margin during the Paleocene-Eocene Thermal Maximum. Paleoceanography 29 (6), 471–488.

Gibbs, S.J., Bown, P.R., Sessa, J.A., Bralower, T.J., Wilson, P.A., 2006a. Nannoplankton extinction and origination across the Paleocene-Eocene Thermal Maximum. Science 314 (5806), 1770–1773.

Gibbs, S.J., Bralower, T.J., Bown, P.R., Zachos, J.C., Bybell, L.M., 2006b. Shelf and open-ocean calcareous phytoplankton assemblages across the Paleocene-Eocene Thermal Maximum; implications for global productivity gradients. Geology 34 (4), 233–236.

Gibbs, S.J., Sheward, R.M., Bown, P.R., Poulton, A.J., Alvarez, S.A., 2018. Warm plankton soup and red herrings: calcareous nannoplankton cellular communities and the Palaeocene–Eocene Thermal Maximum. Philos. Trans. R. Soc. A Math. Phys. Eng. Sci. 376 (2130), 20170075.

Gradstein, F.M., Ogg, J.G., Schmitz, M., Ogg, G.M., 2012. The Geologic Time Scale 2012, Volume 1. Elsevier, 1144 pp.

Gutjahr, M., Ridgwell, A., Sexton, P.F., Anagnostou, E., Pearson, P.N., Pälike, H., Norris, R.D., Thomas, E., Foster, G.L., 2017. Very large release of mostly volcanic carbon during the Palaeocene–Eocene Thermal Maximum. Nature 548 (7669), 573–577.

Handley, L., O'Halloran, A., Pearson, P.N., Hawkins, E., Nicholas, C.J., Schouten, S., McMillan, I.K., Pancost, R.D., 2012. Changes in the hydrological cycle in tropical East Africa during the Paleocene–Eocene Thermal Maximum. Palaeogeogr. Palaeoclimatol. Palaeoecol. 329-330, 10–21.

Hardie, L.A., Eugster, H.P., 1971. The depositional environment of marine evaporites: a case for shallow, clastic accumulation. Sedimentology 16 (3–4), 187–220.

He, D., Jia, C., Li, D., Zhang, C., Meng, Q., Shi, X., 2005. Formation and evolution of polycyclic superimposed Tarim Basin. Oil Gas Geol. 26 (1), 64–77.

IPCC, 2013. Climate Change 2013: The Physical Science Basis. Contribution of Working Group I to the Fifth Assessment Report of the Intergovernmental Panel on Climate Change. United Kingdom and New York, NY, USA, Cambridge.

Ivany, L.C., Pietsch, C., Handley, J.C., Lockwood, R., Allmon, W.D., Sessa, J.A., 2018. Little lasting impact of the Paleocene-Eocene thermal Maximum on shallow marine molluscan faunas. Sci. Adv. 4 (9).

Janssen, Arie W., Sessa, Jocelyn A., Thomas, Ellen, 2016. Pteropoda (Mollusca, Gastropoda, Thecosomata) from the Paleocene-Eocene Thermal Maximum (United States Atlantic Coastal Plain). Palaeontologia Electronica 19.3.47A, pp. 1–26. palaeo-electronica.org/content/2016/1662-pteropoda-from-the-usa-petm.

Jiang, S., Wise Jr., S.W., 2006. Surface-water chemistry and fertility variations in the tropical Atlantic across the Paleocene/Eocene thermal maximum as evidenced by calcareous nannoplankton from ODP Leg 207, Hole 1259B. Rev. Micropaleontol. 49 (4), 227–244.

Jiang, T., Wan, X., Aitchison, J.C., Xi, D., Cao, W., 2018. Foraminiferal response to the PETM recorded in the SW Tarim Basin, central Asia. Palaeogeogr. Palaeoclimatol. Palaeoecol. 506, 217–225.

Jiang, J., Hu, X., Li, J., BouDagher-Fadel, M., Garzanti, E., 2021. Discovery of the Paleocene-Eocene Thermal Maximum in shallow-marine sediments of the Xigaze forearc basin, Tibet: a record of enhanced extreme precipitation and siliciclastic sediment flux. Palaeogeogr. Palaeoclimatol. Palaeoecol. 562, 110095.

Kahn, A., Aubry, M.-P., 2004. Provincialism associated with the Paleocene/Eocene thermal maximum: temporal constraint. Mar. Micropaleontol. 52 (1–4), 117–131.

Keller, G., Mateo, P., Punekar, J., Khozyem, H., Gertsch, B., Spangenberg, J., Bitchong, A. M., Adatte, T., 2018. Environmental changes during the Cretaceous-Paleogene mass extinction and Paleocene-Eocene Thermal Maximum: implications for the Anthropocene. Gondwana Res. 56, 69–89.

Kennett, J.P., Stott, L.D., 1991. Abrupt deep-sea warming, palaeoceanographic changes and benthic extinctions at the end of the Palaeocene. Nature 353 (6341), 225–229.
Khozyem, H., Adatte, T., Spangenberg, J.E., Tantawy, A.A., Keller, G., 2013. Palaeoenvironmental and climatic changes during the Palaeocene–Eocene Thermal Maximum (PETM) at the Wadi Nukhul Section, Sinai, Egypt. J. Geol. Soc. 170 (2), 341–352.
Kiehl, J.T., Shields, C.A., Snyder, M.A., Zachos, J.C., Rothstein, M., 2018. Greenhouse- and orbital-forced climate extremes during the early Eocene. Philos. Trans. R. Soc. A Math. Phys. Eng. Sci. 376 (2130), 20170085.
Lei, Y., Jiang, S., Wise Jr., S.W., Cui, Y., Wang, Y., 2016. Contrasting response of the calcareous nannoplankton communities after the Eocene hyperthermal events in the tropical Atlantic Ocean. Mar. Micropaleontol. 129, 24–31.
Li, J., Hu, X., Garzanti, E., BouDagher-Fadel, M., 2017. Shallow-water carbonate responses to the Paleocene–Eocene thermal maximum in the Tethyan Himalaya (southern Tibet): Tectonic and climatic implications. Palaeogeogr. Palaeoclimatol. Palaeoecol. 466, 153–165.
Li, J., Hu, X., Zachos, J., Garzanti, E., BouDagher-Fadel, M., 2020. Sea level, biotic and carbon-isotope response to the Paleocene–Eocene thermal maximum in Tibetan Himalayan platform carbonates. Glob. Planet. Chang. 103316.
Li, W., Hu, X., Melinte-Dobrinescu, M.C., BouDagher-Fadel, M.K., Li, J., Zhang, S., Xu, Y., 2021. Early Paleogene hyperthermal events and their environmental impacts in the Qimugen section, Tarim Sea. Sci. Bull. 66 (9), 1067–1082 (in Chinese with English abstract).
Li, J., Hu, X., Garzanti, E., BouDagher-Fadel, M., 2022. Spatial heterogeneity in carbonate-platform environments and carbon isotope values across the Paleocene–Eocene thermal maximum (Tethys Himalaya, South Tibet). Glob. Planet. Chang. 214, 103853.
Lippert, P.C., van Hinsbergen, D.J.J., Dupont-Nivet, G., 2014. Early cretaceous to present latitude of the central proto-Tibetan Plateau: A paleomagnetic synthesis with implications for Cenozoic tectonics, paleogeography, and climate of Asia. In: Nie, J., Horton, B.K., Hoke, G.D. (Eds.), Toward an Improved Understanding of Uplift Mechanisms and the Elevation History of the Tibetan Plateau, Geological Society of America. Special Paper, 507, pp. 1–21. https://doi.org/10.1130/2014.2507(01).
López, G.I., 2015. Walther's Law of Facies. In: Jack Rink, W., Thompson, J.W. (Eds.), Encyclopedia of Scientific Dating Methods. Springer, Netherlands, Dordrecht, pp. 957–958.
Lyons, S.L., Baczynski, A.A., Babila, T.L., Bralower, T.J., Hajek, E.A., Kump, L.R., Polites, E.G., Self-Trail, J.M., Trampush, S.M., Vornlocher, J.R., Zachos, J.C., Freeman, K.H., 2019. Palaeocene–Eocene Thermal Maximum prolonged by fossil carbon oxidation. Nat. Geosci. 12 (1), 54–60.
Mao, S., Norris, G., 1984. Late Cretaceous-Early Tertiary dinoflagellates and acritarchs in the western Tarim Basin, Xinjiang. Earth Sci. 2 (2), 7-22+139-141. (in Chinese with English abstract).
Martini, E., 1971. Standard Tertiary and Quaternary calcareous nannoplankton zonation. In: Farinacci, A. (Ed.), Proceedings of the II Planktonic Conference. Edizioni Tecnoscienza, Roma, pp. 739–785, 1970.
McInerney, F.A., Wing, S.L., 2011. The Paleocene-Eocene Thermal Maximum: a perturbation of carbon cycle, climate, and biosphere with implications for the future. Annu. Rev. Earth Planet. Sci. 39, 489–516.
Molnia, B.F., 1974. A rapid and accurate method for the analysis of calcium carbonate in small samples. J. Sediment. Res. 44 (2), 589–590.
Murphy, A.E., Sageman, B.B., Hollander, D.J., Lyons, T.W., Brett, C.E., 2000. Black shale deposition and faunal overturn in the Devonian Appalachian Basin: clastic starvation, seasonal water-column mixing, and efficient biolimiting nutrient recycling. Paleoceanography 15 (3), 280–291.
Mutterlose, J., Linnert, C., Norris, R., 2007. Calcareous nannofossils from the Paleocene-Eocene Thermal Maximum of the equatorial Atlantic (ODP Site 1260B): evidence for tropical warming. Mar. Micropaleontol. 65, 13–31.
Panchuk, K., Ridgwell, A., Kump, L.R., 2008. Sedimentary response to Paleocene-Eocene Thermal Maximum carbon release: a model-data comparison. Geology 36 (4), 315–318.
Penman, D.E., Honisch, B., Zeebe, R.E., Thomas, E., Zachos, J.C., 2014. Rapid and sustained surface ocean acidification during the Paleocene-Eocene Thermal Maximum. Paleoceanography 29 (5), 357–369.
Perch-Nielsen, K., 1985. Cenozoic calcareous nannofossils. In: Bolli, H.M., Saunders, J.B., Perch-Nielsen, K. (Eds.), Plankton Stratigraphy. Cambridge University Press, Cambridge, UK, pp. 427–554.
Ramstein, G., Fluteau, F., Besse, J., Joussaume, S., 1997. Effect of orogeny, plate motion and land–sea distribution on Eurasian climate change over the past 30 million years. Nature 386 (6627), 788–795.
Reif, D.M., Slatt, R.M., 1979. Red bed members of the Lower Triassic Moenkopi Formation, southern Nevada; sedimentology and paleogeography of a muddy tidal flat deposit. J. Sediment. Res. 49 (3), 869–889.
Röhl, U., Westerhold, T., Bralower, T.J., Zachos, J.C., 2007. On the duration of the Paleocene-Eocene thermal maximum (PETM). Geochem. Geophys. Geosyst. 8 (12), Q12002. https://doi.org/10.1029/2007GC001784.
Sagoo, N., Valdes, P., Flecker, R., Gregoire, L.J., 2013. The Early Eocene equable climate problem: can perturbations of climate model parameters identify possible solutions? Philos. Trans. R. Soc. A Math. Phys. Eng. Sci. 371 (2001), 20130123.
Scotese, C., 2014. Atlas of Paleogene Paleogeographic Maps (Mollweide Projection), Maps 8–15, Vol. 1. The Cenozoic, PALEOMAP Atlas for ArcGIS, PALEOMAP Project, Evanston, IL.
Secord, R., Bloch, J.I., Chester, S.G.B., Boyer, D.M., Wood, A.R., Wing, S.L., Kraus, M.J., McInerney, F.A., Krigbaum, J., 2012. Evolution of the earliest horses driven by climate change in the Paleocene-Eocene Thermal Maximum. Science 335 (6071), 959–962.
Self-Trail, J.M., Powars, D.S., Watkins, D.K., Wandless, G.A., 2012. Calcareous nannofossil assemblage changes across the Paleocene-Eocene thermal Maximum: evidence from a shelf setting. Mar. Micropaleontol. 92-93, 61–80.
Self-Trail, J.M., Robinson, M.M., Bralower, T.J., Sessa, J.A., Hajek, E.A., Kump, L.R., Trampush, S.M., Willard, D.A., Edwards, L.E., Powars, D.S., Wandless, G.A., 2017. Shallow marine response to global climate change during the Paleocene-Eocene Thermal Maximum, Salisbury Embayment, USA. Paleoceanogr. Paleoclimatol. 32 (7), 710–728.
Smith, T., Rose, K.D., Gingerich, P.D., 2006. Rapid Asia-Europe-North America geographic dispersal of earliest Eocene primate Teilhardina during the Paleocene-Eocene thermal maximum. Proc. Natl. Acad. Sci. U. S. A. 93 (30), 11223–11227.
Speijer, R.P., Schmitz, B., 1998. A benthic foraminiferal record of Paleocene sea level and trophic/redox conditions at Gebel Aweina, Egypt. Palaeogeogr. Palaeoclimatol. Palaeoecol. 137 (1–2), 79–101.
Speijer, R.P., Wagner, T., 2002. Sea-level changes and black shales associated with the late Paleocene thermal maximum: organic-geochemical and micropaleontologic evidence from the southern Tethyan margin (Egypt-Israel). In: Koeberl, C., MacLeod, K.G. (Eds.), Catastrophic Events and Mass Extinctions: Impacts and beyond, 356. Geological Society of America, pp. 533–549.
Stassen, P., Thomas, E., Speijer, R.P., 2012. Integrated stratigraphy of the Paleocene-Eocene thermal maximum in the New Jersey Coastal Plain: toward understanding the effects of global warming in a shelf environment. Paleoceanography 27 (4). PA4210.
Stassen, P., Dupuis, C., Steurbaut, E., Yans, J., Storme, J.-Y., Morsi, A.-M., Lacumin, P., Speijer, R.P., 2013. Unraveling the Paleocene-Eocene thermal maximum in shallow marine Tethyan environments: the Tunisian stratigraphic record. Newsl. Stratigr. 46 (1), 69–91.
Tang, T., 1992. Marine Sedimentary Characteristics and Sedimentary Environment of Upper Cretaceous to Lower Tertiary in the Western Tarim Basin, Xinjiang. Science Press, Beijing (in Chinese with English abstract).
Thomas, E., 2007. Cenozoic mass extinctions in the deep sea; what perturbs the largest habitat on Earth? Special Paper - Geological Society of America 424, 1–23.
Thomas, E., Shackleton, N.J., 1996. The Paleocene-Eocene benthic foraminiferal extinction and stable isotope anomalies. Geol. Soc. Spec. Publ. 101, 401–441.
Wang, X., Xi, D., Watkins, D.K., Self-Trail, J.M., Tang, Z., Cao, W., Jiang, T., Kamran, M., Wan, X., 2022. Regression of the Tethys Sea (central Asia) during middle to late Eocene: evidence from calcareous nannofossils of western Tarim Basin, NW China. Mar. Micropaleontol. 171, 102085.
Westerhold, T., Röhl, U., Laskar, J., 2012. Time scale controversy: accurate orbital calibration of the early Paleogene. Geochem. Geophys. Geosyst. 13 (6).
Wierzbowski, H., 2007. Effects of pre-treatments and organic matter on oxygen and carbon isotope analyses of skeletal and inorganic calcium carbonate. Int. J. Mass Spectrom. 268 (1), 16–29.
Winguth, A., Shellito, C., Shields, C., Winguth, C., 2010. Climate response at the paleocene-eocene thermal maximum to greenhouse gas forcing-a model study with CCSM3. J. Clim. 23 (10), 2562–2584.
Yao, W., Paytan, A., Wortmann, U.G., 2018. Large-scale ocean deoxygenation during the Paleocene-Eocene Thermal Maximum. Science 361 (6404), 804-+.
Zachos, J.C., Wara, M.W., Bohaty, S., Delaney, M.L., Petrizzo, M.R., Brill, A., Bralower, T.J., Premoli-Silva, I., 2003. A transient rise in tropical sea surface temperature during the Paleocene-Eocene Thermal Maximum. Science 302 (5650), 1551–1554.
Zachos, J.C., Rohl, U., Schellenberg, S.A., Sluijs, A., Hodell, D.A., Kelly, D.C., Thomas, E., Nicolo, M., Raffi, I., Lourens, L.J., McCarren, H., Kroon, D., 2005. Rapid acidification of the ocean during the Paleocene-Eocene thermal maximum. Science 308 (5728), 1611–1615.
Zeebe, R.E., Dickens, G.R., Ridgwell, A., Sluijs, A., Thomas, E., 2014. Onset of carbon isotope excursion at the Paleocene-Eocene thermal maximum took millennia, not 13 years. Proc. Natl. Acad. Sci. U. S. A. 111 (12), E1062–E1063.
Zeebe, R.E., Ridgwell, A., Zachos, J.C., 2016. Anthropogenic carbon release rate unprecedented during the past 66 million years. Nat. Geosci. 9 (4), 325–329.
Zhang, Z., Wang, H., Guo, Z., Jiang, D., 2007. What triggers the transition of palaeoenvironmental patterns in China, the Tibetan Plateau uplift or the Paratethys Sea retreat? Palaeogeogr. Palaeoclimatol. Palaeoecol. 245 (3), 317–331.
Zhang, Q., Wendler, I., Xu, X., Willems, H., Ding, L., 2017. Structure and magnitude of the carbon isotope excursion during the Paleocene-Eocene thermal maximum. Gondwana Res. 46, 114–123.
Zhang, S., Hu, X., Han, Z., Li, J., Garzanti, E., 2018. Climatic and tectonic controls on Cretaceous-Palaeogene Sea-level changes recorded in the Tarim epicontinental sea. Palaeogeogr. Palaeoclimatol. Palaeoecol. 501, 92–110.
Zhang, Q., Willems, H., Ding, L., Xu, X., 2019. Response of larger benthic foraminifera to the Paleocene-Eocene thermal maximum and the position of the Paleocene/Eocene boundary in the Tethyan shallow benthic zones: evidence from south Tibet. Geol. Soc. Am. Bull. 131 (1–2), 84–98.
Zhong, S., 1984. Coccolithophores from the cretaceous Kukebai Formation in the western Tarim Basin, Xinjiang. Acta Micropaleontol. Sin. 1 (2), 201-206+223-224. (in Chinese with English abstract).
Zhou, X., Thomas, E., Rickaby, R.E.M., Winguth, A.M.E., Lu, Z., 2014. I/Ca evidence for upper ocean deoxygenation during the PETM. Paleoceanography 29 (10), 964–975.
Zhu, J., Poulsen, C.J., Tierney, J.E., 2019. Simulation of Eocene extreme warmth and high climate sensitivity through cloud feedbacks. Sci. Adv. 5 (9), eaax1874.
Zhu, J., Poulsen, C.J., Otto-Bliesner, B.L., Liu, Z., Brady, E.C., Noone, D.C., 2020. Simulation of early Eocene water isotopes using an Earth system model and its implication for past climate reconstruction. Earth Planet. Sci. Lett. 537, 116164.